CARBON 70 (2014) 295–307

Available at www.sciencedirect.com

ScienceDirect

journal homepage: www.elsevier.com/locate/carbon

# Mesoporous carbon nanofibers with large cage-like pores activated by tin dioxide and their use in supercapacitor and catalyst support

*Zhaoyang Liu* [1], *Dongying Fu* [1], *Feifei Liu*, *Gaoyi Han* [*], *Cuixian Liu*, *Yunzhen Chang*, *Yaoming Xiao*, *Miaoyu Li*, *Sidian Li*

*Institute of Molecular Science, Key Laboratory of Chemical Biology and Molecular Engineering of Education Ministry, Shanxi University, Taiyuan 030006, China*

ARTICLE INFO

*Article history:*
Received 2 July 2013
Accepted 7 January 2014
Available online 13 January 2014

ABSTRACT

The mesoporous carbon nanofibers (MCFs) with large cage-like pores have been fabricated by thermally treating electrospun fibers of polyvinyl alcohol containing tin compound. During the process, tin oxide is reduced to melting tin and the carbon is activated to form the porous carbon. The results of X-ray diffraction and transmission electron microscopy at different temperatures show that particles of $SnO_2$ (~1.9 nm) exist in the fibers at 300 °C while mixtures of Sn and SnO with rod-like shapes appear in the matrix when the fibers are heated at 400 °C, and that Sn migrates to the surface of fibers and pores are formed in the fibers at higher temperature. Specific surface area of MCFs can reach 800 $m^2 g^{-1}$ and the average diameter of interior pores is about 10.3 nm while the entrance pores are small. The specific capacitance of MCFs is 105 F $g^{-1}$ and the fabricated symmetrical capacitors exhibit high-rate capacitive properties and excellent stability, Pt nanoparticles which can be densely loaded on MCFs exhibit relatively high activity and stability toward electrooxidation of methanol, which indicate that MCFs may be used as electrodes for high-rate energy storage and support for catalyst. This approach may be extended to prepare other porous carbon materials.



## 1. Introduction

Considerable efforts have been made to the synthesis, modification and application of the mesoporous materials due to their large specific surface area and porous structure [1–3] since the ordered mesoporous molecular sieve was successful synthesized in 1992 [4]. Among mesoporous materials, mesoporous carbons (MPCs) have attracted much attention because of their high conductivity, large specific surface area, electrochemical stability and low cost can meet requirements of the applications in catalyst supports, energy storage and conversion systems, adsorbents, membrane separations and templates for other materials [5,6]. Up to date, many methods have been developed to control the pore structure in carbon [7]. For example, the porous carbon has been prepared [8] by carbonizing the ion exchange resin containing cations (Ca, Fe, Ni, Cu, Zn, K and Na). The highly mesoporous activated carbon fiber has been prepared by steam invigorating the pitch fibers at 850 °C in the presence of rare-earth metal complexes or by using catalytic activation [9–11]. Furthermore, MPCs can also been fabricated by using inorganic templates (mesoporous $SiO_2$ or $SiO_2$ particles, etc.) and organic templates (surfactant, liquid–crystal, polyethylene glycol and triblock copolymers) through pyrolyzing various organic

* *Corresponding author:* Fax: +86 351 7016358.
E-mail address: han_gaoyis@sxu.edu.cn (G. Han).
[1] These authors contributed equally to this work.
0008-6223/$ - see front matter 
http://dx.doi.org/10.1016/j.carbon.2014.01.011

compounds [12–17]. Generally, MPCs fabricated by using ordered templates have a narrow pore size distribution while the porous carbon prepared at high temperature by using zinc chloride, potassium hydroxide, potassium carbonate and water vapor as activators exhibits more micropores instead of mesopores and possesses a wide pore size distribution [18–20].

Besides the electrical conductivity, MPCs can provide large interface of electrode/ electrolyte for electrostatic charge accumulation and the large surface area for dispersion of catalysts [21–24]. As one kind of capacitors, electric double-layer capacitor (EDLC) depends mainly on the accumulation of charges at the interface of electrode/electrolyte. The use of MPCs in EDLC has stimulated much interest due to their mesoporous structure, high specific surface area and the moderate cost [25–28] although many other carbon materials such as carbon nanotubes (CNTs), carbon nanofibers (CNFs), ordered mesoporous carbons (OMCs) and graphene, etc. have been widely used as the materials of electrodes for capacitors [29–31]. Direct methanol fuel cell (DMFC), a kind of energy conversion device, is considered as promising power source for the next-generation portable electronic device [32,33]. Generally, the catalysts used in DMFC are loaded on supports in order to make the catalyst particles highly dispersed [34–37]. For example, having synthesized OMCs by using mesoporous silica as template, Joo et al. have found that OMCs can load Pt particles as high as 60 wt.% with high dispersion [24]. Kim et al. have used hollow carbon spheres with mesoporous on the shell to increase the catalyst utilization [36]. In addition to the above-mentioned Pt catalyst, the bi-metallic catalyst of Pt–Ru has also been loaded on OMCs to improve the performance of catalyst in DMFC [37].

Recently, electrospinning is considered as a new method to fabricate nanosized carbon materials. The electrospinning-derived carbon fibres and composite fibers such as Si/C, $Fe_3O_4$/C, $SnO_2$/C and Sn/C [38–41] have been fabricated and used in supercapacitor, catalyst supports and anodic materials for Li-ion batteries owing to their three-dimensional porous-connected structure and relatively large surface area [42–48]. For example, the activity and stability of Pt particles have been improved [42–44] by using the electrospinning-derived carbon fibers as support. In order to increase the specific surface area further, porous carbon nanofibers have been fabricated by thermally treating the composite fibers of polymers, in which one of the polymers such as polymethylmethacrylate or polyvinylpyrrolidone or other inorganic component ($SiO_2$ and $ZnCl_2$, etc.) acts as pore-forming reagents [46–48]. However, few literatures about the mesoporous corbon nanofibers (MCFs) prepared by using $SnO_2$ as activator have been reported.

As mentioned above, the MPCs prepared by using template require templates and the post-processing is complex although the distribution of pore size is narrow [24]. The porous carbon materials prepared at high temperature by using activators such as KOH exhibit mainly the micropores [30,49,50], and there is difficulty to recover the element of K due to the volatility at high temperature. Therefore, it is interesting to find new system for preparation of MPCs. Considering that $SnO_2$ can be reduced easily through carbon-thermal reaction and that Sn has a low-melting point (231.9 °C) and a high-boiling point (2260 °C) which are favorable to its recovery, the tin compound may be used as activator to prepare porous carbon materials. In this paper, the MCFs with large cage-like pores have been fabricated by combining the electrospinning and thermally treating the composite fibers containing tin precursor. During the process of thermal treatment, $SnO_2$ is reduced to Sn along with the consumption of carbon, the melting Sn migrates out of the carbon fibers, and then the mesopores are formed in the carbon fibers.

## 2. Experimental section

### 2.1. Fabrication of the materials

The synthesis of the tin precursor was described briefly as follows: firstly, 3.0 g $SnCl_4{\cdot}5H_2O$ was dissolved into 20 mL deionized water under stirring, then 6.0 mL ammonia was dropped into the solution slowly to make the white precipitate formed. The white precipitate was collected and washed with large amount of water after lasting for 1 h. Subsequently, the obtained product was transferred into 10 mL solution of citric acid (0.2 g $mL^{-1}$) and treated under ultrasonic condition for 10 min. Then the transparent solution was obtained and saved for use after being heated for about 5 min. The solution for electrospinning was prepared by dissolving polyvinyl alcohol (PVA, $M_w$ = 80,000) into the tin-citric solution at 90 °C under stirring to form a solution of PVA (100 mg $mL^{-1}$). Then the solution was transferred into a plastic pipette with an inner diameter of about 1.0 mm after the addition of 4 μL Triton X-100. A thin platinum rod connected to a high-voltage power supply was put into the plastic pipette. The potential for electrospinning was kept at +15 kV, and the resulted fibers were collected on a sheet of electrically grounded aluminum foil which was 13 cm below the plastic pipette tip. The mats were peeled off the aluminum foil and dried under vacuum at 100 °C for 12 h and then pre-oxidized at air for 2 h. The brown mats were then placed into a tube furnace for carbonization under high-purity Ar atmosphere. The temperature was firstly increased to 300 °C at a heating rate of 13 °C $min^{-1}$ and kept for 5 min, and then to 600 °C at heating rate of 15 °C and kept for 10 min, finally to 1200 °C at heating rate of 10 °C and kept at this temperature for 2 h. After cooling, the obtained black products were treated by concentrated hydrochloric acid to remove the residual Sn. Finally, the MCFs were obtained after they were washed by water repeatedly and dried at 100 °C for 24 h. In order to compare the porous structure of the fibers, the pre-oxidized mats were also carbonized under high-purity Ar atmosphere at 1200 °C but with different heating rates such as 5, 7.5, 10 and 15 °C $min^{-1}$. The obtained black products at heating rate of 5 °C $min^{-1}$ were named as MiCFs after they were treated by the similar procedure to MCFs. In order to clarify the change of the composite fibers at different

temperatures, the samples were also prepared at different such temperatures as 300, 400, 500 and 650 °C for 10 min with a heating rate of 15 °C $min^{-1}$.

### 2.2. Characterization

The micromorphologies of the product were observed by using a scanning electron microscope (SEM, JEOL-JSM-6701F) operating at an accelerating voltage of 10 kV and a transmission electron microscope (TEM, JEOL-JEM-1011) operating at an accelerating voltage of 200 kV. X-ray diffraction (XRD) patterns were recorded on a Bruker D8 Advance X-ray diffractometer (Cu Kα) in the $2\theta$ range of 10–80° with a scan rate of 5° $min^{-1}$. The X-ray photoelectron spectroscopy (XPS) was performed on a PHI5300 ESCA/610SAM spectrometer under a pressure lower than $10^{-8}$ torr with Al Kα radiation as the exciting source. Nitrogen adsorption–desorption isotherms were measured at 77 K on a Micromeritics ASAP 2000 volumetric adsorption system. The Brunauer–Emmett–Teller (BET) specific surface area of the samples was calculated from nitrogen adsorption data in the relative pressure ranging from 0.04 to 0.18. The total pore volume was estimated from the amount of nitrogen adsorbed at a relative pressure of about 0.99. The micropore surface area and the micropore volume were estimated from nitrogen adsorption data using the t-plot method. The mesopore size was calculated using the Brunauer–Joyner–Hallenda (BJH) method while the micropore size was calculated by using Horvath–Kawazoe method. The thermogravimetric analysis (TGA) was performed on a STA449C thermo gravimetric analyzer from room temperature to 800 °C with a heating rate of 20 °C $min^{-1}$ under $N_2$ atmosphere.

### 2.3. The capacitive properties

Firstly, two nearly identical (in weight and size, 6 × 6 mm) pieces of MCFs or MiCFs with a thickness of about 30 μm were immersed in 6.0 mol $L^{-1}$ KOH aqueous solution under vacuum in order to make pores filled with electrolyte. The two slices of MCFs or MiCFs were separated by filter paper adsorbed with 6.0 mol $L^{-1}$ KOH aqueous solution, and then two Pt foils were used as the current collectors. All the components were assembled into a sandwiched structure between two plastic sheets. The assembled two-electrode capacitor was used to measure the capacitive performance. The measurements of cyclic voltammetry (CV) at different scan rates and galvanostatic charge/discharge at different current densities were conducted in the potential window of −0.60 to 0.60 V and carried out on an electrochemical workstation CHI660C (Shanghai, Chenhua). The electrochemical impedance spectroscopy (EIS) was also recorded in the frequency-range of $10^{-2}$–$10^{5}$ Hz under an open-circuit model with ac-voltage amplitude of 5 mV. The specific capacitance ($C_{sc}$) of the samples based on one electrode can be calculated [31] on the basis of CV curves according to following equation:

$$C_{sc} = \left(\int IdV\right)/(\upsilon m \Delta V) \quad (1)$$

where $I$ is the response current (A), $\Delta V$ the difference of potential during the CV tests (V), $\upsilon$ the potential scan rate (V $s^{-1}$), and $m$ the mass of the materials used in one electrode (g).

Furthermore, the $C_{sc}$, power density and energy density can also be calculated from the galvanostatic charge/discharge curves [51]. For example, the $C_{sc}$ can be obtained by using the equation based on the discharged curves:

$$C_{cs} = 2(I\Delta t/m\Delta V) \quad (2)$$

where $I$ represents the constant discharge current (A), $\Delta t$ the discharging time (s), m the mass of one electrode (g), and $\Delta V$ the voltage drop upon discharging (V). Then the energy density and power density of the EDLCs depicted in the Ragone plot can be calculated by using the formula:

$$E = (1/8)C_{cs}\Delta V^2 \quad (3)$$

$$P = E/\Delta t \quad (4)$$

### 2.4. The properties of MCFs used as the support of catalyst

Generally, the as-prepared MCFs were ground into powders before use. A certain amount of $H_2PtCl_6{\cdot}6H_2O$ (6.0 mg Pt) was dissolved into 20 mL water under stirring, then 7.0 mL aqueous solution of $NaBH_4$ (0.03 mol $L^{-1}$) was slowly adding into the mixture and the color of the mixture changed from light yellow to brown. Then MCFs powders (1.5, 4.0 and 9.0 mg) dispersed in 2.0 mL water were poured into the Pt colloidal solution and kept stirring for 1 h. Finally, the catalyst was collected by vacuum filtration, washed by water thoroughly and dried under vacuum at 90 °C for 2 h after the same amount of $NaBH_4$ solution was added into the mixture again and kept stirring for additional 1 h. The catalysts containing 40%, 60% and 80% Pt were defined as Pt/MCF-40, Pt/MCF-60 and Pt/MCF-80, respectively. For comparison, the catalyst containing 60% Pt was also prepared by using MiCFs as support and defined as Pt/MiCF-60, and the Pt catalyst supported on carbon black Vulcan XC-72 (220 $m^2$ $g^{-1}$) with a Pt loading of 40% was purchased from Johnson Matthey Corp and named as Pt/C-40. The electrodes for the electro-catalytic test were fabricated by loading the Pt/MCF on carbon paper. The ultrasonic-treated mixture containing certain amount of Pt/MCF catalyst, water (0.6 mL) and Nafion solution (0.1 mL) was transferred onto carbon paper, the solvent was then evaporated at the room temperature. The content of Pt in all the electrodes was determined by using an IRIS Advantage inductively coupled plasma atomic emission spectroscopy system and kept about 0.25 mg $cm^{-2}$, and the geometric surface area of the electrodes was guaranteed to be about 0.04 $cm^2$.

The performance of the electrocatalyst for methanol electrooxidation was measured by using a three-electrode system in 0.5 mol $L^{-1}$ $H_2SO_4$ + 1.0 mol $L^{-1}$ $CH_3OH$ aqueous solution at 25 °C. The strips of carbon paper loaded with catalysts, Pt plate and saturated calomel electrode (SCE) were used as working, counter and reference electrode, respectively. The EIS was carried out in the frequency ranging from $10^{-2}$ to $10^{5}$ Hz with amplitude of 5 mV at different potentials. High-purity $N_2$ was used to deaerate the solutions and maintained above the electrolyte during measurements.

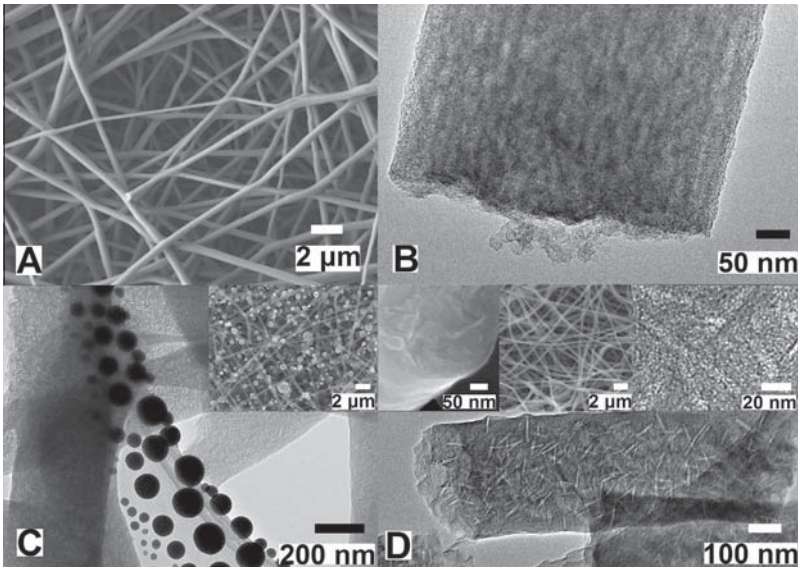


**Fig. 1 – The SEM image (A) and TEM image (B) of the PVA/Sn-citric composite fibers after pre-oxidation at 200 °C, the TEM images of the composite fibers after being heated at 1200 °C (C, inserted figure: SEM image) and after being removed Sn by hydrochloric acid (D, insets: cross-section, general SEM image and the magnified TEM image).**

## 3. Results and discussion

### 3.1. *The characterization of the products*

From the SEM image shown in Fig. 1A, it is found that the composite fibers of PVA/Sn-citric treated at 200 °C spread randomly and exhibit smooth surface, and that many gaps are observed between the fibers. However, the TEM image (Fig. 1B) reveals that many small particles disperse in the matrix of the fibers, and that the particles are not uniformly dispersed in the fibers but some aggregates have appeared. After being heated at 1200 °C, many pores arrayed randomly in the fiber have also been found besides many particles ranged from tens of nanometers to several microns on the surface of the fibers (Fig. 1C). However, the large Sn particles dispersed on the fibers' surface disappear, and the elongated pores with the diameter of about 8–15 nm in the fibers matrix can be easily observed (Fig. 1D) after the composite has been treated by hydrochloride acid. Furthermore, it can be found that the ends of the pores have smaller diameters than the interior of pores. The cross-section SEM image (inserted figure) also shows the pores dispersed randomly in the fiber. From the high-resolution TEM image of the fiber (inserted figure), it can be found clearly that many pores with the average size of about 0.9 nm spread in the fiber.

The TEM images show that the MiCFs prepared at heating rate of 5.0 °C $min^{-1}$ exhibit mainly micropores and less macropores (Fig. 2A and Fig. S1). However, the samples prepared at heating rate of 7.5 °C $min^{-1}$ exhibit more mesopores (Fig. 2B) and the diameter of pores becomes smaller compared with MiCFs. It is interesting to find that the pores become longer with the increase of the heating rates. For example, the diameter and length of the pores in the fibers prepared at heating rate of 15 °C $min^{-1}$ are smaller and longer (Fig. 2D) than that in the fibers prepared at the heating rate of 7.5 and 10 °C $min^{-1}$ (Fig. 2B and C). From Figs. 1D 2D, it is also found that the formation of long-shaped pores is favorable when samples are heated at 300 °C and 600 °C for certain time. These results indicate that the pyrolysis of the PVA/Sn-citric is an interesting method to prepare carbon materials because the products with different porous structures can be easily obtained by controlling the heating conditions.

In order to clarify the changes of the composite during the thermally treating, XRD patterns of the samples prepared at different temperatures are recorded and shown in Fig. 3. It is found that $SnO_2$ appears mainly in the fibers prepared at 300 °C and the average size of the $SnO_2$ particles is calculated to be about 1.9 nm according to the Scherrer formula. It is interesting to find that the mixture of SnO and Sn emerges in the fibers when the samples are treated at 400 °C, and that tin oxide has been completely reduced to Sn when the treated temperature is higher than 500 °C. This results is similar to the previous literature [41] in which Sn is formed by thermally treating the composite fibers containing $SnCl_2$ at 500 °C for 3 h. However, it is found that tin oxide can be reduced to Sn at temperature as low as 400 °C in this work. According to the TGA curves (Fig. S2), it is clear that the composite fibers have more weight loss compared with the PVA fibers due to the consumption of carbon caused by the reduction of tin oxide. In fact, the yields of the carbon from the composites are only about 10%.

The SEM images (Fig. S3) show that the fibers treated at 300 °C have a smooth surface, and that the surface of the fibers heated at 400 °C exhibits some large particles but more large particles exhibit on the surface of fiber after the fibers are heated at 500 °C. These results demonstrate that metallic Sn has formed and flowed out at 400 °C due to its low melting-point. From the TEM images of the samples prepared at different temperatures, it is clear that many small particles of $SnO_2$ have dispersed in the matrix of fiber treated at 300 °C (Fig. 4A) and the diameter of the particles is consistent to the result obtained from XRD. Compared with Fig. 1B, it can be seen that

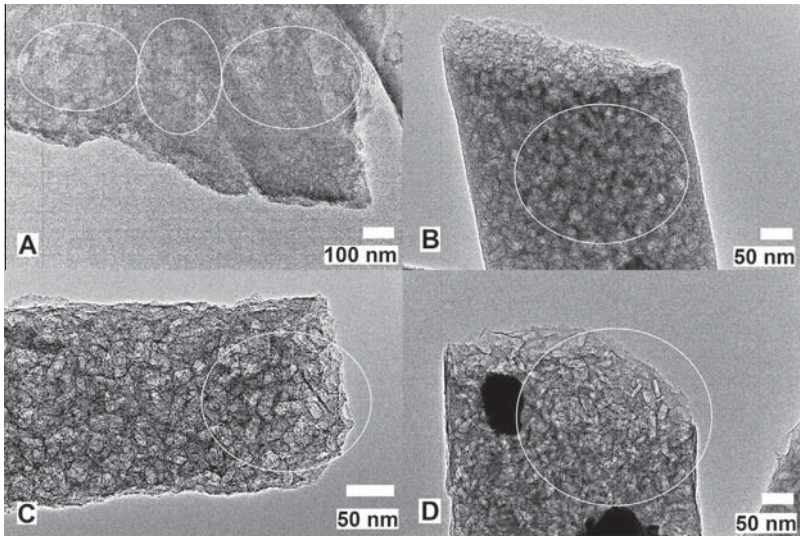


**Fig. 2 – The TEM image of the porous carbon fibers prepared at different heating rates. 5 (A), 7.5 (B), 10 (C) and 15 °C min$^{-1}$ (D).**

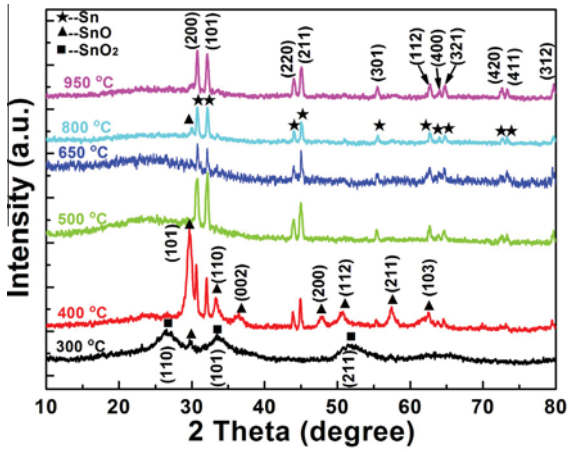


**Fig. 3 – The XRD pattern of the composite fibers after being heated at different temperature. (A color version of this figure can be viewed online.)**

the particles exhibit more congregations. After the fibers are heated at 400 °C (Fig. 4B), the size and shape of the particles in the fiber exhibit an obvious difference compared with Fig. 4A. For example, besides some large particles dispersed on the surface of the fibers, there are many particles with elongate shape in the fiber. Furthermore, it can be seen that some elongate pores have formed in the fiber. More pores and more large particles can be observed in the fiber (Fig. 4C) and on the fiber's surface respectively when the treated temperature increases to 500 °C. Finally, the fiber thermally treated at 650 °C shows clearer elongate pores (Fig. 4D) and fewer particles on the fiber's surface compared with the sample prepared at 500 °C. According to the results obtained from XRD and TEM, it may be deduced that the pores are formed as follows: firstly, the Sn-citric precursor disperses in the PVA solution uniformly, then the particles of precursor are formed and dispersed in the fibers during the process of electrospinning. However, the particles dispersed in the fibers are not absolutely uniform and some domains contain more particles due to the rapid drying or phase separation during spinning process. During the heating process, the small $SnO_2$ particles and some SnO particles are formed and they congregate in some region with high concentration of particles due to the migration of the particles. With the increase of the temperature, $SnO_2$ particles react with the organic matrix to form some SnO particles and then migrate in the fiber to form the micropores. When the temperature reaches to 400 °C, part of SnO is reduced to melting Sn because the temperature is higher than the melting-point of Sn, then mixture of melting tin and SnO forms more compact congregates with elongate shape and migrates in fiber. Finally, SnO is completely reduced to Sn with the consumption of carbon and the melting Sn will flow out of the fiber and then cohere outside the fibers because of the large surface tension of metal when the temperature reaches to 500 °C. Therefore the elongate mesopores are formed in the carbon fibers due to the consumption of carbon and the flow of the melting Sn. Why have the different pores formed at different heating rates? According to the measurements and factors that the tin oxide has been completely reduced to tin at 500 °C and tin has a low-melting point, the consumption of carbon and the migration of the nanoparticles of tin oxide at low temperature may contribute to the formation of micropores. When the heating rate is as low as 5 °C min$^{-1}$, the migration rate of the particles (tin oxide and melting tin) can be matched with the reaction between tin oxide and carbon, therefore the formed tin congregates slowly in the carbon matrix to form the large agglomerate firstly and then flows out of the fibers to form macropores. Considering that the tin can be generated in the fiber is constant, the number of the formed large agglomerates is less in this case, so micropores together with some macropores are observed in the carbon fibers. However, when the heating rate is as high as 15 °C min$^{-1}$, the time of the whole reaction between tin oxide and carbon is only one-third of that 5 °C min$^{-1}$, the migration rate of the particles (tin oxide and melting tin) is lower than the formation rate of melting tin, therefore, melting tin together with the formed gas congregate in the carbon

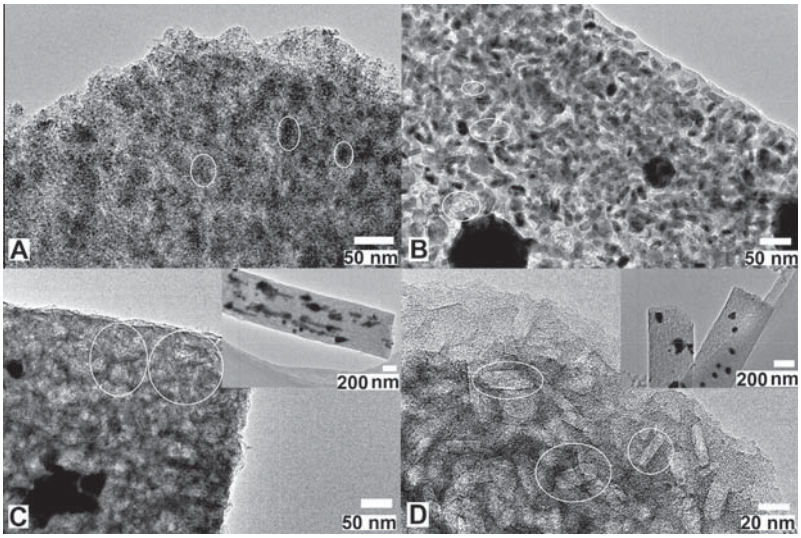


**Fig. 4 – The TEM images of the composite fibers treated at different temperature. 300 (A), 400 (B), 500 (C) and 650 °C (D). The inserted figures in C and D are the low magnified TEM images of the fibers.**

matrix to form large amount of small agglomerates in a short time. Subsequently, the formed small aggregates extrude out of the carbon fibers quickly, in this case, many mesopores with elongate shape are generated besides the micropores.

The nitrogen adsorption–desorption isotherms of MCFs and MiCFs are shown in Fig. 5A. It is clear that the isotherm (Fig. 5A-a) of MCFs reveals a typical characteristic of Type IV (H2). Multilayer adsorption that takes place at lower pressures

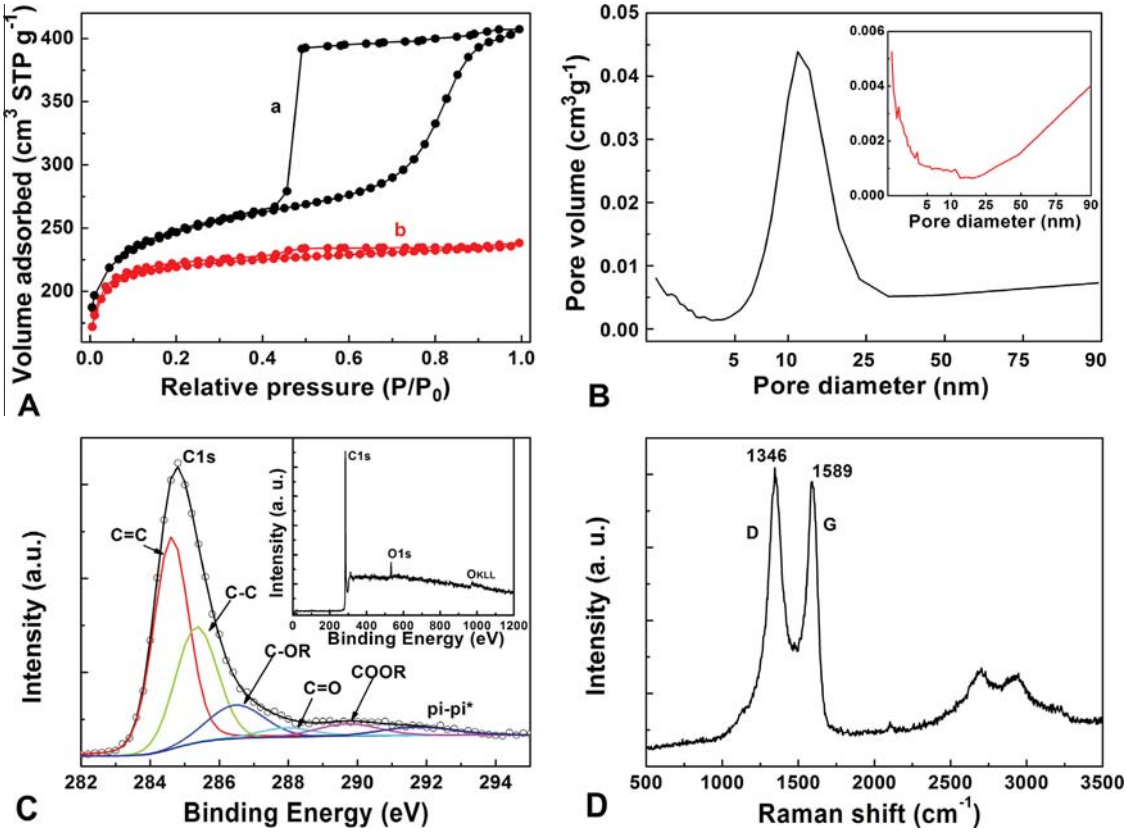


**Fig. 5 – The nitrogen adsorption and desorption isotherms of (a) MCFs (b) and MiCFs (A, the isotherm corresponding to MCFs is offset vertically by 20 $cm^3 g^{-1}$), the curves of pore volume versus mesopore size estimated from adsorption branch of $N_2$ isotherms for MCFs (B, the inserted figure is the curve for MiCFs), the C1s XPS spectrum (C, the inset is the general XPS spectrum of the CFMs) and the Raman spectrum of MCFs (D). (A color version of this figure can be viewed online.)**

is followed by the capillary condensation at the relative pressure range of 0.65–0.90. Adsorption–desorption isotherm for smaller pores is reversible, but an obvious hysteresis in the isotherm is observed for the range of larger pore diameters, which reveals the characteristic of materials with large cage-like mesopores (small entrances and large interiors) [52]. Such judgment is based on the following fact: the capillary evaporation occurred at a relative pressure of 0.45–0.50 possesses a significant delay compared with the capillary condensation, which is very different from the narrow hysteresis loops observed in the adsorption–desorption isotherms of the uniform channel-like mesoporous materials [53]. However, the isotherm of MiCFs (Fig. 5A-b) shows very different features, there is not capillary condensation observed. From Fig. 5B, it can be found that MCFs exhibit larger pore volume in the range of mesopore than MiCFs. Furthermore, the pore size distribution plots (Fig. S5) show that MCFs possess micropores of less than 1 nm and the mesopores with an average diameter of 10.3 nm [54], and that MiCFs possess mainly micropores of less than 1 nm and a small amount of macropores. These results are consistent with those observed by TEM and the structural properties of the samples calculated on the basis of nitrogen adsorption data are listed in Table 1. It is found that the specific surface area of MCFs (800 $m^2 g^{-1}$) is slightly greater than that of MiCFs (778 $m^2 g^{-1}$). However, CFMs exhibit much larger total pore volume, external and mesopore surface area than MiCFs.

The XPS spectrum reveals that the surface of the MCFs is dominated by carbon and oxygen (95.77 at.% of C and 4.23 at.% of O), which demonstrates that the Sn has been removed completely. The O1s data show the presence of two fitted peaks (Fig. S4) located at about 532.4 and 533.7 eV, which are contributed to the carbonyl oxygen atoms in esters, anhydrides and the oxygen atoms in hydroxyls or ethers (532.4 eV), and the oxygen related to carboxyl group (533.7 eV) [55]. The C1s XPS data (Fig. 5C) reveal that the kinds of carbon bond are mainly C=C or C—C species (284.6 and 285.2 eV) along with a small amount of C—OR, C=O and O=C—OR which are located at 286.4, 287.6 and 289.2 eV, respectively. Additionally, the peak located at 291.2 eV is usually assigned as the satellite peak (p–p*) of carbon [56,57]. The Raman spectrum (Fig. 5D) presents the D band at 1346 $cm^{-1}$ and the G band at 1589 $cm^{-1}$, the ratio of surface area of D band to G band is calculated to be about 1.96, indicating that the MCFs exhibit many defects and less crystalline [42].

### 3.2. *The capacitive properties*

From the CV curves recorded at the operating potential between −0.60 and 0.60 V at different scan rates (Fig. 6A and B), it is found that unobvious redox waves appear in the CV curves except that the CV profile shows a hump at the low potential at low scan rate of 5 mV $s^{-1}$, which may be attributed to the contribution of the redox reactions of the active functional groups on the surface of the materials. The CV curves possess the typical rectangular shape at a relatively low scan rates, but they slightly deviate from the rectangular shape with the increment of the scan rates due to the restricted motion of electrolyte in the pores at high scan rate [58,59]. It is interesting to find that the profile of the CV for MCFs still keeps a quasi-rectangular shape with a small distortion at scan rate of 2000 mV $s^{-1}$, indicating that the cell prepared by CFMs possesses remarkable high-rate capability. However, the CV curves for the capacitor fabricated by MiCFs (Fig. 6C and D) can only keep quasi-rectangular shape at scan rates lower than 400 mV $s^{-1}$, and deviate obviously from the rectangular shape when the scan rate reaches to 2000 mV $s^{-1}$. These results indicate that the good capacitive properties of MCFs may result from their mesoporous structure.

The galvanostatic charge/discharge curves (Fig. S6) of the capacitors assembled by MCFs show that all the curves are highly symmetrical and linear with unobvious *iR* drops at small current densities, and that the *iR* drop increases obviously with the increase of the current density at large currenties. The repeated charge/discharge curves of the cell of MCFs at current density of 20 A $g^{-1}$ show a less deviation from the cutoff potential of 0.60 and −0.60 V (Fig. S7), indicating that the cell prepared by CFMs has an excellent stability. In contrast, the galvanostatic charge/discharge curves for the capacitor prepared by MiCFs (Fig. S8) show much larger *iR* drop compared with MCFs at the same current density. According to the formula 1, the $C_{cs}$ of MCFs and MiCFs can reach to 105 and 100 F $g^{-1}$ at scan rate of 5 mV $s^{-1}$, respectively. The values of volumetric capacitance for MCFs and MiCFs are also calculated and found to be about 43.1 and 41 F $cm^{-3}$ respectively according to the data of $C_{cs}$ and density (0.41 g $cm^{-3}$). The $C_{cs}$ of MCFs and MiCFs are higher than that of some mesoporous carbon [14] and CNTs [60] but lower than that of some porous carbon materials with very large surface area [61], which may be caused by the high treating temperature or not high surface area. The $C_{cs}$ values decrease with the increase of the scan rates, but MCFs exhibit slighter trend compared with MiCFs. For example, MCFs retain 55% of the initial $C_{cs}$ at high scan rate of 2000 mV $s^{-1}$ (Fig. S9A), which is much better than MiCFs (23%) and better than many carbon materials previously reported [46–48]. Furthermore, the $C_{cs}$ of MCFs calculated from the discharged curves decreases gradually from 103 (1 A $g^{-1}$) to 62 F $g^{-1}$(100 A $g^{-1}$), and the charge/discharge efficiency ($t_{discharge}$/tcharge × 100%) decreases from about 93 (1 A $g^{-1}$) to 66% (100 A $g^{-1}$) (Fig. S9B), which is much better than that of MiCFs (Fig. S10A) and indicate that the assembled capacitor has excellent capacitive behavior due to the efficient formation of double-layer in the interface of electrolyte/electrode. The large difference in the capacitive properties between MCFs and MiCFs may mainly come from their structural characteristics. It is well known that the capacitive properties of EDLC depend on the surface area and the porous structure of the materials. The MCFs and MiCFs have a similar specific surface area based on BET method (about 800 $m^2 g^{-1}$), so they possess a similar $C_{cs}$ at low scan rate of 5 mV $s^{-1}$ (about 100 F $g^{-1}$). However, the MCFs exhibit more mesopores, much larger mesopore surface and external surface area than MiCFs, which make the electrolyte diffusion in the MCFs easier than in MiCFs. Therefore, the MCFs exhibit relatively high $C_{cs}$ and good high-rate capacitive properties.

In order to validate the promising applications of MCFs in electrochemical capacitors, the Ragone plot of the symmetrical capacitors based on the data from discharged curves is shown in Fig. 7A. According to the discharged curves (excluding the *iR* drops), it is found that the capacitors exhibit an

**Table 1 – Structural properties of the samples calculated on the basis of nitrogen adsorption data.**

| Sample | $S_{BET}$ ($m^2\ g^{-1}$) | $V_t$ ($cm^3\ g^{-1}$) | $S_{mi}$ ($cm^2\ g^{-1}$) | $V_{mi}$ ($cm^3\ g^{-1}$) | $S_{ex+me}$ |
|---|---|---|---|---|---|
| MCFs | 800 | 0.60 | 361 | 0.17 | 439 |
| MiCFs | 778 | 0.37 | 590 | 0.30 | 188 |

$S_{BET}$, BET specific surface area; $V_t$, total pore volume; $S_{mi}$, micropore surface area; $V_{mi}$, micropore volume; $S_{ex+me}$, external and primary mesopore surface area.

energy density of 5.1 Wh $kg^{-1}$ and a power density of 242.2 W $kg^{-1}$ at current density of 1 A $g^{-1}$, and 2.0 Wh $kg^{-1}$ and 16.0 kW $kg^{-1}$ at current density of 100 A $g^{-1}$. Cyclic life is another important requirement for capacitors. From the cyclic stability of the capacitor assembled by MCFs shown in Fig. 7B, it is clear that the $C_{cs}$ value has almost not changed during the 4250 cyclic tests. Initially, the $C_{cs}$ has some slight increase, but it tends to keep stable at the successive test period and only 1% fluctuation for $C_{cs}$ may be ascribed to the collapse of pores and the changes of the surface functional groups. The CV curves recorded at 1st, 2015th and 4200th cycle are almost the same, especially that the 2015th and 4200th curves are almost completely overlapping (inset in Fig. 7B), which also reveals the excellent stability.

From the Nyquist plots shown in Fig. 8A, it is found that the capacitors assembled by CFMs before (a) and after (b) the stability test display a small semicircle at high frequency followed by a transition to linearity at low frequency. The semicircles at higher frequency region are related to the process of the charge-transfer at the electrode/electrolyte interface, and the slope of lines at lower frequency region should be ascribed to the diffusion of the electrolyte ions in the electrode pores [62]. The vertical lines close to 90° at low frequency suggest the pure capacitive behavior and fast transfer character of electrolyte ions in the electrode [63]. The smaller semicircle after the test of stability reveals more efficient contact between the electrolyte and the surface of MCFs. Fig. 8B presents the capacitance obtained from the EIS before (a) and after (b) stability test, the capacitance of the MCFs decreases with the increase of the frequency and behaves like a pure resistance in high-frequency region, which indicates that the electrolyte ions cannot be diffused in the carbon material [64] to form the EDLC at high frequency. It is also found that after stability test the material exhibits a slightly higher $C_{cs}$ at low frequency range. It should be noted that the $C_{cs}$ values of the capacitor cell at 0.01 Hz are

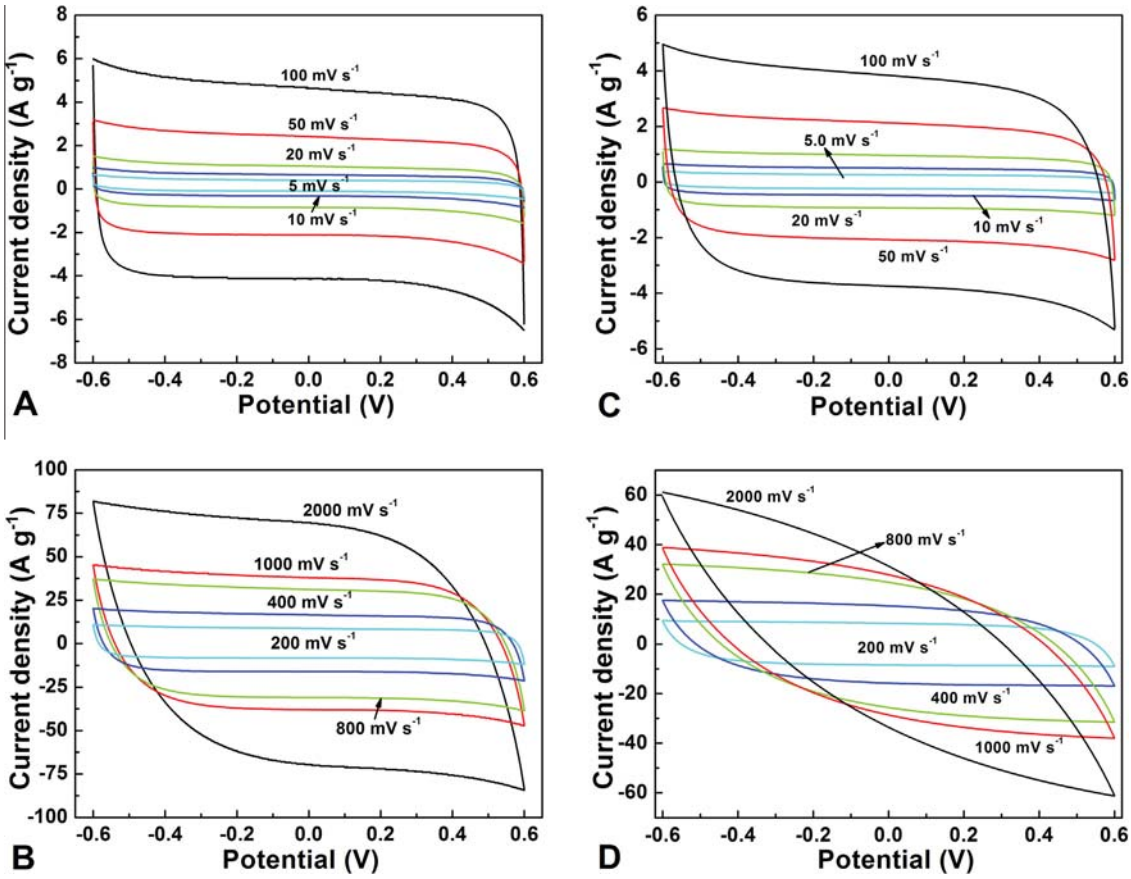


**Fig. 6 – The CV curves of the capacitor assembled by the MCFs (A and B) and MiCFs (C and D) recorded at low scan rates (A and C) and at high scan rates (B and D). (A colour version of this figure can be viewed online.)**

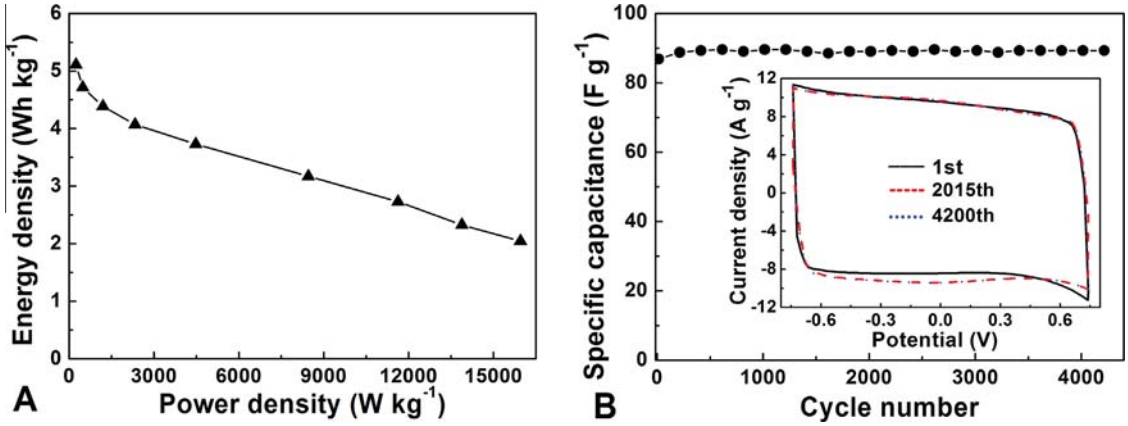


**Fig. 7 – Ragone plots of the energy density versus power density calculated according to discharged curves (A), and the cyclic stability of capacitor assembled by MCFs (B) upon repeated scans at 150 mV $s^{-1}$, the inserted figure shows the CV curves recorded at 1st, 2015th and 4200th cycle. (A color version of this figure can be viewed online.)**

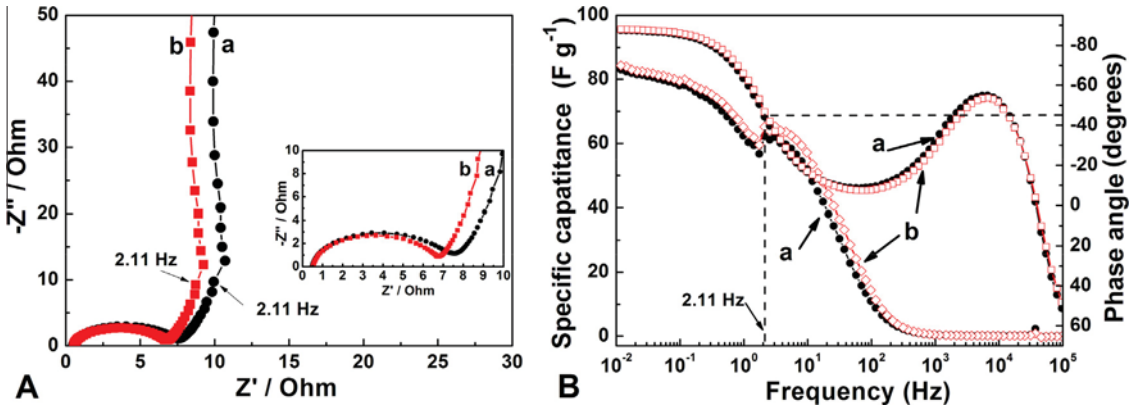


**Fig. 8 – Complex plot of the capacitor assembled by MCFs and the inset shows the high-frequency region of the plot (A) and the plots of specific capacitance of MCFs and the phase angles versus the frequency (B). (A color version of this figure can be viewed online.)**

deviated from that derived from CV and charge/discharge test, which is mainly due to the different testing systems applied. In Fig. 8B, the characteristic frequency $f_0$ for phase angle of −45° marks the point at which the resistive and capacitive impedances are equal [63]. The $f_0$ (2.11 Hz) provides a time constant $\tau_0$ ($1/f_0$) which tells how fast the device can be reversibly charged and discharged [46,51]. The $\tau_0$ for the capacitor fabricated by MCFs is about 0.47 s which is smaller than that of MiCFs (1.56 s, Fig. S10B) and the ordered mesoporous carbons previously reported [61]. This character also demonstrates that the MCFs have the high-rate capability.

### 3.3. *The properties of samples used as support for catalyst*

The prepared carbon fibers are also used as support to load Pt catalyst for electrooxidation of methanol. The XRD patterns shown in Fig. 9A reveal that the CMFs exhibit a broad diffraction peak at about 25° which corresponds to the diffraction of C (002) plane (Fig. 9A-a). Besides the diffraction of C(002), the Pt catalysts supported on carbon show three diffraction peaks at 39.8°, 46.4° and 67.6°, which are corresponding to the diffraction of Pt (111), (200) and (220) crystal plane. Using the Scherrer formula, the average diameters of Pt particles are calculated to be about 5.57, 5.38, 5.34 and 3.58 nm for Pt/MCF-40, Pt/MCF-60, Pt/MCF-80 and Pt/C-40 based on the diffraction peak of Pt (111), respectively. The Pt 4f XPS spectra (Fig. 9B) show that the Pt particles dispersed on the support of carbon exhibit $Pt^{2+}$ and $Pt^{4+}$ species besides the $Pt^0$ species. Compared with bulk Pt, it is found that the binding energy for Pt $4f_{7/2}$ shifts to high-region. Furthermore, it can also be found that the binding energy for Pt $4f_{7/2}$ in Pt/C-40 is slightly higher than that of Pt/MCF, indicating that MCFs have less ability to attract the electrons of Pt. Furthermore, the samples have the similar C1s XPS spectra (Fig. S11) and Raman spectra (Fig. S12).

From the TEM images, it is found that partial Pt particles are dispersed on the surface of the fibers, but other Pt particles are loaded on the surface of the fibers as conglomeration for Pt/MCF-80 (Fig. S13A). In comparison with the catalysts of Pt/MCF-80 and 60, the Pt particles in Pt/MCF-40 have less conglomeration and the size of the conglomeration is relatively small (Fig. S13B and C). The commercial Pt/C-40 catalyst shows a uniform dispersion of Pt particles on the surface of carbon particles, the sizes of the Pt particles are clearly

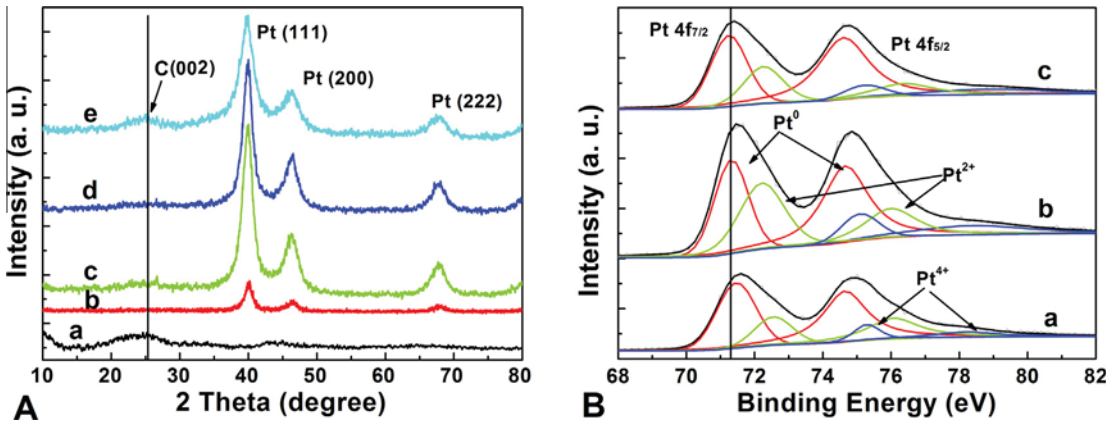


**Fig. 9 – (A) The XRD patterns of MCFs (a), Pt/MCF-40 (b), Pt/MCF-60 (c), Pt/MCF-80 (d) and commercial Pt/C-40 (e), (B) the Pt XPS spectra of commercial, Pt/C-40 (a), Pt/MCF-80 (b) and Pt/MCF-60 (c). (A color version of this figure can be viewed online.)**

smaller than that supported on MCFs (Fig. S13D). The size of the Pt particles observed from TEM images is consistent with the size of the Pt particles obtained from XRD patterns. From the TEM image of Pt/MiCFs-60, it is found that the Pt particles supported on MiCFs are relatively uniform and the size of Pt particles is about 5.2 nm (Fig. S14), which is similar to that on MCFs.

As shown in Fig. 10A, all of the catalysts have a current peak for methanol oxidation at about 0.70–0.73 V (vs. SCE) during the positive scan ($I_f$), while the other current peak at about 0.45–0.50 V at negative sweep ($I_b$) is corresponding to the oxidation of the incompletely oxidized carbonaceous species which have formed in the positively going potential scan. The maximum current density for methanol oxidation during positive sweep is about 323, 262, 219, 251 and 202 mA $mg^{-1}$ Pt for Pt/MCF-80, Pt/MCF-60, Pt/MCF-40, Pt/MiCF-60 and Pt/C-40, respectively. The value of $I_f/I_b$ is about 1.03 for electrode of Pt/MCF-80 loading on carbon paper which is higher than those for Pt/MiCF-60 (1.01), Pt/MCF-60 (0.99), Pt/MCF-40 (0.91) and commercial Pt/C-40 (0.87), indicating that more intermediate carbonaceous species are oxidized to carbon dioxide in the positively going scan on Pt/MCF-80 [65]. The optimum activity of Pt supported on MCFs is lower than Pt on electrospinning-derived carbon fibers [42–44], graphene–$CeO_2$ [66] hybrid and graphene–$MnO_2$ hybrid [67] due to the poor distribution of Pt on MCFs, but the activity is larger than that on reduced graphene oxide [68,69] prepared through microwave-assisted or by femtosecond laser pulses. It is considered that the activity of catalyst is related with its electrochemical active surface area (ECSA). So the data of ECSA for the Pt particles loaded on carbons are determined according to the hydrogen adsorption–desorption CV curves (Fig. S15) recorded in deaerated 0.5 mol $L^{-1}$ $H_2SO_4$ aqueous solution at sweep rate of 50 mV $s^{-1}$. Using the value of 0.21 mC $cm^{-2}$ for a clean Pt electrode [42], the ECSAs of the catalysts are calculated by integrating the area within the region of –0.24 to 0.1 V under the hydrogen desorption wave and found to be 23.7, 19.0, 19.3, 22.1 and 23.2 $m^2$ $g^{-1}$ for Pt/MCF-80, Pt/MCF-60, Pt/MCF-40, Pt/MiCF-60 and Pt/C-40, respectively. In order to obtain the activity on unit ECSA, the peak current densities of the methanol oxidation have been normalized by the ECSA of Pt nanoparticles. It is found that the activities toward methanol oxidation based on ECSAs are 1.36, 1.37, 1.15, 1.13 and 0.87 mA $cm^{-2}$ for Pt/MCF-80, Pt/MCF-60, Pt/MCF-40, Pt/MiCF-60

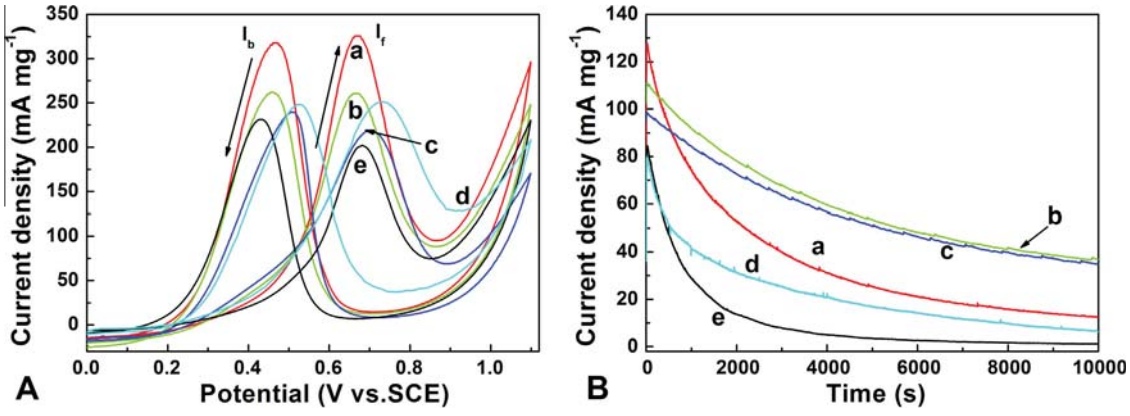


**Fig. 10 – (A) CV curves for methanol oxidation on (a) Pt/MCF-80, (b) Pt/MCF-60, (c) Pt/MCF-40, (d) Pt/MiCF-60 and (e) Pt/C-40 electrodes at scan of 50 mV $s^{-1}$, (B) The chronoamperometric curves of methanol oxidation on (a) Pt/MCF-80, (b) Pt/MCF-60, (c) Pt/MCF-40, (d) Pt/MiCF-60 and (e) Pt/C-40 electrodes at a constant potential of 0.45 V. Electrolyte: $N_2$ saturated 0.5 mol $L^{-1}$ $H_2SO_4$ + 1.0 mol $L^{-1}$ $CH_3OH$ aqueous solution. (A color version of this figure can be viewed online.)**

and Pt/C-40, respectively. The results also indicate that the activity of Pt particles towards methanol oxidation can be improved by loading on MCFs.

In the practical application, the stability of the catalyst is as important as the activity of the catalyst, so the polarized current density for methanol oxidation is determined at a constant potential of 0.45 V for 10,000 s, from which it can be seen that the current densities for methanol oxidation continue decay with the increase of the experimental time after reaching their maxima (Fig. 10B). For example, the current densities decrease to about 84.0, 91.6, 74.0 41.2 and 28.8 mA $mg^{-1}$ Pt after a polarization time of 1000 s, while decrease to about 34.8, 37.2, 12.8 6.5 and 1.2 mA $mg^{-1}$ Pt after 10,000 s test for Pt/MCF-40, Pt/MCF-60, Pt/MCF-80, Pt/MiCF-60 and commercial Pt/C-40, respectively. The current densities retain about 35.2%, 34.6%, 9.8%, 8.1% and 1.5% of the maximum current densities for Pt/MCF-40, Pt/MCF-60, Pt/MCF-80, Pt/MiCFs and commercial Pt/C-40, respectively. It is thought that Pt/MCF-60 exhibits excellent performance in both the activity and stability considering that the activity and the retained current density on Pt/MCF-60 are larger than that on Pt/MCF-40 although the retained current density on Pt/MCF-40 is slightly larger. These results show that the optimum catalyst supported on the MCFs exhibits better stability than Pt particles supported on electrospinning-derived carbon fibers [43,44], and that the stability is comparable to Pt particles supported on the reduced graphene oxide [68] and the hybrids of carbon–graphene [42], graphene–$CeO_2$ [66] and graphene–$MnO_2$ [67].

The charge transfer resistance ($R_{ct}$) obtained from the EIS can give the kinetic information about the methanol oxidation [65,70]. From the EIS spectra recorded at 0.35 V, the $R_{ct}$ values are evaluated as 13.1, 23.3, 40.2 and 57.3 Ω $cm^2$ for catalysts of Pt/MCF-80, Pt/MCF-60, Pt/MCF-40 and Pt/C-40 loaded on the carbon paper (Fig. S16). Such result shows clearly that a rather quick charge transfer rate has realized on Pt/CFM electrode during methanol electro-oxidation. It is generally considered that the small Pt particles with good dispersion on support exhibit higher activity and stability to methanol electro-oxidation than large particles and aggregates, but the results obtained in this paper are different. These differences may result from: (1) it is unavoidable that a significant portion of Pt/C particles is detached from the substrate and isolated from the electrical circuit even with the most advanced electrodes prepared by wetting–drying method, resulting in a low Pt utilization [71], (2) the MCFs in the layer of catalyst have a good contact between each other and form the large pores due to the relatively long size of MCFs, which satisfy the requirements of reactant access, proton access, and electronic continuity for electro-catalyst, (3) the mesoporous carbon structure is usually considered to be an ideal catalyst support for electrode support materials in DMFC because it can provide favorable hosting morphology for the metallic catalyst clusters and interconnected pore network for a facile transport of feeds and products [72]. On the other hand, that MCFs contain many pores with large interior and small entrance on the surface may make the Pt particles anchored on the fibers' surface with more pores and limit the movement of the particles during the electrochemical tests.

## 4. Conclusions

A feasible method to prepare the mesoporous carbon fibers with cage-like pores has been developed by combining the electrospinning technique and thermal treatment. The obtained carbon material exhibits high specific surface area and relatively uniform mesopores. The electrochemical measurements show that the capacitor assembled by MCFs exhibits excellent quick charge/discharge properties, and that the specific capacitance of it can reach to about 105 F $g^{-1}$. Furthermore, the MCFs used as catalyst support can load catalyst in large amount. The Pt catalyst at high loading of 80% has the maximum current density toward methanol oxidation, while the catalyst of Pt/MCF-60 possesses the good activity and very high stability. This method developed for preparation of the MCFs with large cage-like pores is easy and efficient and can be extended to prepare other mesoporous carbon materials.

## Acknowledgements

The authors thank the National Natural Science Foundation of China (21274082 and 21073115) and Shanxi province (2012021021-3), the Program for New Century Excellent Talents in University (NCET-10-0926) of China and the Program for the Top Young and Middle-aged Innovative Talents of Shanxi province (TYMIT), and the returned personnel of scientific research project of Shanxi (2011-003).

## Appendix A. Supplementary data

Supplementary data associated with this article can be found, in the online version, at http://dx.doi.org/10.1016/j.carbon.2014.01.011.

## REFERENCES

[1] Davis ME. Ordered porous materials for emerging applications. Nature 2002;417:813–21.
[2] Corma A. From microporous to mesoporous molecular sieve materials and their use in catalysis. Chem Rev 1997;97:2373–419.
[3] Wan Y, Zhao DY. On the controllable soft-templating approach to mesoporous silicates. Chem Rev 2007;107:2821–60.
[4] Kresge CT, Leonowicz ME, Roth WJ, Vartuli JC, Beck JS. Ordered mesoporous molecular sieves synthesized by a liquid-crystal template mechanism. Nature 1992;359:710–2.
[5] Hartmann M. Ordered mesoporous materials for bioadsorption and biocatalysis. Chem Mater 2005;17:4577–93.
[6] Lee J, Kim J, Hyeon T. Recent progress in the synthesis of porous carbon materials. Adv Mater 2006;18:2073–94.
[7] Tyotani T. Control of pore structure in carbon. Carbon 2002;38:269–86.
[8] Nakagawa H, Watanabe K, Harada Y, Miura K. Control of micropore formation in the carbonized ion exchange resin by utilizing pillar effect. Carbon 1999;37:1455–61.
[9] Tamai H, Kojima S, Ikeuchi M, Mondori J, Kanata T, Yasuda H. Synthesis of extremely large mesoporous activated carbon

and its unique adsorption for giant molecules. Chem Mater 1996;8:454–62.
[10] Tamai H, Ikeuchi M, Kojima S, Yasuda H. Extremely large mesoporous carbon fibers synthesized by the addition of rare earth metal complexes and their unique adsorption behaviors. Adv Mater 1997;9:55–8.
[11] Freman JJ, Gimblett FGR, Roberts RA, Sing KSW. Studies of activated charcoal cloth. III. Mesopore development induced by phosphate impregnants. Carbon 1988;26:7–11.
[12] Ryoo R, Joo SH, Jun S. Synthesis of highly ordered carbon molecular sieves via template- mediated structural transformation. J Phys Chem B 1999;103:7743–6.
[13] Ryoo R, Joo SH, Kruk M, Jaroniec M. Ordered mesoporous carbons. Adv Mater 2001;13:677–81.
[14] Qiao ZA, Guo BK, Binder AJ, Chen JH, Veith GM, Dai S. Controlled synthesis of mesoporous carbon nanostructures via a "silica-assisted" strategy. Nano Lett 2013;13:207–12.
[15] Zhai YP, Dou YQ, Liu XX, Tu B, Zhao DY. One-pot synthesis of magnetically separable ordered mesoporous carbon. J Mater Chem 2009;19:3292–300.
[16] Huang Y, Cai HQ, Feng D, Gu D, Deng YH, Tu B, et al. One-step hydrothermal synthesis of ordered mesostructured carbonaceous monoliths with hierarchical porosities. Chem Commun 2008;23:2641–3.
[17] Ozaki J, Endo N, Ohizumi W, Igarashi K, Nakahara M, Oya A. Novel preparation method for the production of mesoporous carbon fiber from a polymer blend. Carbon 1997;35:1031–3.
[18] Gorka J, Zawislak A, Choma J, Jaroniec M. KOH activation of mesoporous carbons obtained by soft-templating. Carbon 2008;46:1159–74.
[19] Girgis BSAN, El-Hendawy A. Porosity development in activated carbons obtained from date pits under chemical activation with phosphoric acid. Micropor Mesopor Mater 2002;52:105–17.
[20] Budinova T, Ekinci E, Yardim F, Grimm A, Bjornbom E, Minkova V, et al. Characterization and application of activated carbon produced by $H_3PO_4$ and water vapor activation. Fuel Process Technol 2006;87:899–905.
[21] Jiang H, Lee PS, Li CZ. 3D carbon based nanostructures for advanced supercapacitors. Energy Environ Sci 2013;6:41–53.
[22] Zhong MJ, Kim EK, McGann JP, Chun SE, Whitacre JF, Jaroniec M, et al. Electrochemically active nitrogen-enriched nanocarbons with well-defined morphology synthesized by pyrolysis of self-assembled block copolymer. J Am Chem Soc 2012;134:14846–57.
[23] Sharma S, Pollet BG. Support materials for PEMFC and DMFC electrocatalysts – a review. J Power Sources 2012;208: 96–119.
[24] Joo SH, Pak C, You DJ, Lee SA, Lee HI, Kim JM, et al. Ordered mesoporous carbons (OMC) as supports of electrocatalysts for direct methanol fuel cells (DMFC): effect of carbon precursors of OMC on DMFC performances. Electrochim Acta 2006;52:1618–26.
[25] Chen LF, Zhang XD, Liang HW, Kong MG, Guan QF, Chen P, et al. Synthesis of nitrogen-doped porous carbon nanofibers as an efficient electrode material for supercapacitors. ACS Nano 2012;6:7092–100.
[26] Dhawale DS, Benzigar MR, Wahab MA, Anand C, Varghese S, Balasubramanian VV, et al. Fine tuning of the supercapacitive performance of nanoporous carbon electrodes with different pore diameters. Electrochim Acta 2012;77:256–61.
[27] Chen YZ, Wang BP, Dong SJ, Wang YP, Liu YN. Rectangular microscale carbon tubes with protuberant wall for high-rate electrochemical capacitors. Electrochim Acta 2012;80:34–40.
[28] Wang YC, Tao SY, An YL. Superwetting monolithic carbon with hierarchical structure as supercapacitor materials. Micropor Mesopor Mater 2012;163:249–58.
[29] Zhang H, Cao GP, Yang YS. Carbon nanotube arrays and their composites for electrochemical capacitors and lithium-ion batteries. Energy Environ Sci 2009;2:932–43.
[30] Barranco V, Lillo-Rodenas MA, Linares-Solano A, Oya A, Pico F, Ibanez J, et al. Amorphous carbon nanofibers and their activated carbon nanofibers as supercapacitor electrodes. J Phys Chem C 2010;114:10302–7.
[31] Yan J, Wei T, Shao B, Ma FQ, Fan ZJ, Zhang ML, et al. Electrochemical properties of graphene nanosheet/carbon black composites as electrodes for supercapacitors. Carbon 2010;48:1731–7.
[32] Olah GA. Beyond oil and gas: the methanol economy. Angew Chem Int Ed 2005;44:2636–9.
[33] Winter M, Brodd RJ. What are batteries, fuel cells and supercapacitors? Chem Rev 2004;104:4245–69.
[34] Su FB, Zeng JH, Bao XY, Yu YS, Lee YL, Zhao XS. Preparation and characterization of highly ordered graphitic mesoporous carbon as a Pt catalyst support for direct methanol fuel cells. Chem Mater 2005;17:3960–7.
[35] Selvam P, Kuppan B. Synthesis, characterization and electrocatalytic properties of nano-platinum-supported mesoporous carbon molecular sieves, Pt/NCCR-41. Catal Today 2012;198:85–91.
[36] Kim JH, Fang BZ, Yoon SB, Yu JS. Hollow core/mesoporous shell carbon capsule as an unique cathode catalyst support in direct methanol fuel cell. Appl Catal B: Environ 2009;88:368–75.
[37] Salgado JRC, Alcaide F, Alvarez G, Calvillo L, Lazaro MJ, Pastor E. Pt–Ru electrocatalysts supported on ordered mesoporous carbon for direct methanol fuel cell. J Power Sources 2010;195:4022–9.
[38] Ji LW, Zhang XW. Fabrication of porous carbon/Si composite nanofibers as high-capacity battery electrodes. Electrochem Commun 2009;11:1146–9.
[39] Wang L, Yu Y, Chen PC, Zhang DW, Chen CH. Electrospinning synthesis of C/$Fe_3O_4$ composite nanofibers and their application for high performance lithium-ion batteries. J Power Sources 2008;183:717–23.
[40] Yu Y, Gu L, Wang CL, Dhanabalan A, Aken PAV, Maier J, et al. Encapsulation of Sn@carbon nanoparticles in bamboo-like hollow carbon nanofibers as an anode material in lithium-based batteries. Angew Chem Int Ed 2009;48:6485–9.
[41] Zou L, Gan L, Kang FY, Wang MX, Shen WC, Huang ZH. Sn/C non-woven film prepared by electrospinning as anode materials for lithium ion batteries. J Power Sources 2010;195:1216–20.
[42] Chang YZ, Han GY, Li MY, Gao F. Graphene-modified carbon fiber mats used to improve the activity and stability of Pt catalyst for methanol electrochemical oxidation. Carbon 2011;49:5158–65.
[43] Li MY, Chang YZ, Han GY, Yang BS. Platinum nanoparticles supported on electrospinning-derived carbon fibrous mats by using formaldehyde vapor as reducer for methanol electrooxidation. J Power Sources 2011;196:7973–8.
[44] Li MY, Zhao SZ, Han GY, Yang BS. Electrospinning-derived carbon fibrous mats improving the performance of commercial Pt/C for methanol oxidation. J Power Sources 2009;191:351–6.
[45] Cavaliere S, Subianto S, Savych I, Jones DJ, Roziere J. Electrospinning: designed architectures for energy conversion and storage devices. Energy Environ Sci 2011;4:4761–86.
[46] Ma C, Song Y, Shi JL, Zhang DQ, Zhai XL, Zhong M, et al. Preparation and one-step activation of microporous carbon nanofibers for use as supercapacitor electrodes. Carbon 2013;51:290–300.
[47] Wang PQ, Zhang D, Ma FY, Ou Y, Chen QN, Xie SH, et al. Mesoporous carbon nanofibers with a high surface area

electrospun from thermoplastic polyvinylpyrrolidone. Nanoscale 2012;4:7199–204.
[48] Kim BH, Yang KS, Ferraris JP. Highly conductive, mesoporous carbon nanofiber web as electrode material for high-performance supercapacitors. Electrochim Acta 2012;75:325–31.
[49] Xu B, Wu F, Su YF, Cao GP, Chen S, Zhou ZM, et al. Competitive effect of KOH activation on the electrochemical performances of carbon nanotubes for EDLC: balance between porosity and conductivity. Electrochim Acta 2008;53:7730–5.
[50] Zhu YW, Murali S, Stoller MD, Ganesh KJ, Cai WW, Ferreira PJ, et al. Carbon-based supercapacitors produced by activation of graphene. Science 2011;332:1537–41.
[51] Zhang L, Shi GQ. Preparation of highly conductive graphene hydrogels for fabricating supercapacitors with high rate capability. J Phys Chem C 2011;115:17206–12.
[52] Matos JR, Kruk M, Mercuri LP, Jaroniec M, Zhao L, Kamiyama T, et al. Ordered mesoporous silica with large cage-like pores: structural identification and pore connectivity design by controlling the synthesis temperature and time. J Am Chem Soc 2003;125:821–9.
[53] Kruk M, Jaroniec M. Argon adsorption at 77 K as a useful tool for the elucidation of pore connectivity in ordered materials with large cage-like mesopores. Chem Mater 2003;15:2942–9.
[54] Kim TW, Ryoo R, Kruk M, Gierszal KP, Jaroniec M, Kamiya S, et al. Tailoring the pore structure of SBA-16 silica molecular sieve through the use of copolymer blends and control of synthesis temperature and time. J Phys Chem B 2004;108:11480–9.
[55] Zhao H, Han GY, Chang YZ, Li MY, Li YP. The capacitive properties of amorphous manganese dioxide electrodeposited on different thermally-treated carbon papers. Electrochim Acta 2013;91:50–7.
[56] Okpalugo TIT, Papakonstantinou P, Murphy H, McLaughlin J, Brown NMD. High resolution XPS analysis of chemical functionalised multi-wall carbon nanotubes (MWCNTs) and single wall carbon nanotubes. Carbon 2005;43:153–61.
[57] Zielke U, Huttinger KJ, Hoffman WP. Surface-oxidized carbon fibers: I. Surface structure and chemistry. Carbon 1996;34:983–98.
[58] Wang LH, Toyoda M, Inagaki M. Dependence of electric double layer capacitance of activated carbons on the types of pores and their surface areas. New Carbon Mater 2008;23:111–5.
[59] Sheng ZM, Wang JN, Ye JC. Synthesis of nanoporous carbon with controlled pore size distribution and examination of its accessibility for electrode double layer formation. Micropor Mesopor Mater 2008;111:307–13.
[60] Ervin MH, Miller BS, Hanrahana B, Mailly B, Palacios T. A comparison of single-wall carbon nanotube electrochemical capacitor electrode fabrication methods. Electrochim Acta 2012;65:37–43.
[61] Xing W, Qiao SZ, Ding RG, Li F, Lu GQ, Yan ZF, et al. Superior electric double layer capacitors using ordered mesoporous carbons. Carbon 2006;44:216–24.
[62] Wang WH, Wang XD. Investigation of Ir-modified carbon felt as the positive electrode of an all-vanadium redox flow battery. Electrochim Acta 2007;52:6755–62.
[63] Ghaemi M, Ataherian F, Zolfaghari A, Jafari SM. Charge storage mechanism of sonochemically prepared $MnO_2$ as supercapacitor electrode: effects of physisorbed water and proton conduction. Electrochim Acta 2008;53:4607–14.
[64] Jin M, Han GY, Chang YZ, Zhao H, Zhang HY. Flexible electrodes based on polypyrrole/manganese dioxide/polypropylene fibrous membrane composite for supercapacitor. Electrochim Acta 2011;56:9838–45.
[65] Pozio A, Francesco MD, Cemmi A, Cardellini F, Giorgi L. Comparison of high surface Pt/C catalysts by cyclic voltammetry. J Power Sources 2002;105:13–9.
[66] Yu SP, Liu QB, Yang WS, Han KF, Wang ZM, Zhu H. Graphene–$CeO_2$ hybrid support for Pt nanoparticles as potential electrocatalyst for direct methanol fuel cells. Electrochim Acta 2013;94:245–51.
[67] Huang HJ, Chen Q, He MY, Sun XQ, Wang X. A ternary Pt/$MnO_2$/graphene nanohybrid with an ultrahigh electrocatalytic activity toward methanol oxidation. J Power Sources 2013;239:189–95.
[68] Kundu P, Nethravathi C, Deshpande PA, Rajamathi M, Giridhar M, Ravishankar N. Ultrafast microwave-assisted route to surfactant-free ultrafine Pt nanoparticles on graphene: synergistic co-reduction mechanism and high catalytic activity. Chem Mater 2011;23:2772–80.
[69] Chang HW, Tsai YC, Cheng CW, Lin CY, Wu PH. Preparation of graphene-supported platinum nanoparticles in aqueous solution by femtosecond laser pulses for methanol oxidation. J Power Sources 2013;239:164–8.
[70] Yu EH, Scott K, Reeve RW. A study of the anodic oxidation of methanol on Pt in alkaline solutions. J Electroanal Chem 2003;547:17–24.
[71] Liu XM, Li MY, Han GY, Dong JH. The catalysts supported on metallized electrospun polyacrylonitrile fibrous mats for methanol oxidation. Electrochim Acta 2010;55:2983–90.
[72] Nam JH, Jang YY, Kwon YU, Nam JD. Direct methanol fuel cell Pt–carbon catalysts by using SBA-15 nanoporous templates. Electrochem Commun 2004;6:737–41.